Nanoscale morphological evolution of monocrystalline Pt surfaces during cathodic corrosion

Nakkiran Arulmozhi[a], Thomas J. P. Hersbach[a,1], and Marc T. M. Koper[a,2]

[a]Leiden Institute of Chemistry, Leiden University, 2300 RA Leiden, The Netherlands

Edited by Alexis T. Bell, University of California, Berkeley, CA, and approved October 20, 2020 (received for review August 12, 2020)

This paper studies the cathodic corrosion of a spherical single crystal of platinum in an aqueous alkaline electrolyte, to map out the detailed facet dependence of the corrosion structures forming during this still largely unexplored electrochemical phenomenon. We find that anisotropic corrosion of the platinum electrode takes place in different stages. Initially, corrosion etch pits are formed, which reflect the local symmetry of the surface: square pits on (100) facets, triangular pits on (111) facets, and rectangular pits on (110) facets. We hypothesize that these etch pits are formed through a ternary metal hydride corrosion intermediate. In contrast to anodic corrosion, the (111) facet corrodes the fastest, and the (110) facet corrodes the slowest. For cathodic corrosion on the (100) facet and on higher-index surfaces close to the (100) plane, the etch pit destabilizes in a second growth stage, by etching faster in the (111) direction, leading to arms in the etch pit, yielding a concave octagon-shaped pit. In a third growth stage, these arms develop side arms, leading to a structure that strongly resembles a self-similar diffusion-limited growth pattern, with strongly preferred growth directions.

electrochemistry | cathodic corrosion | platinum | self-similar growth

Cathodic corrosion is an electrochemical process in which a metallic electrode undergoes structural surface transformation upon cathodic polarization (1–3). The process is the basis of a synthetic route for nanoparticle production because it does not require the use of surfactants or elaborate synthesis protocols (2–5). Besides, cathodic corrosion has direct relevance to improving the performance and the lifetime of electrochemical systems for hydrogen production (6), CO_2 valorization (7), energy storage and conversion, sensors, and other electrochemical devices (8, 9). However, the atomistic aspects of the structural transformation and the surface evolution during cathodic corrosion are still poorly understood. So far, experiments using polycrystalline wires (10–17) have shown that the corrosion is anisotropic, and the surface roughening generated by cathodic corrosion is more pronounced around grain boundaries (14). The extent of roughness may, therefore, vary depending on the crystallographic distribution (11–13), electrolyte properties (14, 15), and the pretreatment of the electrode (13). However, experiments using polycrystalline electrodes limit detailed fundamental understanding of cathodic corrosion.

In contrast, monocrystalline electrodes are the surfaces of choice to study the atomic scale's structural transformation process (18, 19). Studying cathodic corrosion on monocrystalline surfaces allows tracking the changes from a well-defined atomic structure to a corroded (roughened) surface and correlates the surface etch patterns obtained in the polycrystalline and monocrystalline electrode (20–23). Such an atomistic understanding may ultimately guide approaches to avoid cathodic corrosion or to design procedures to make tailored nanoparticles via cathodic corrosion.

In this contribution, we report on the structural transformation and the surface evolution of Pt(111), Pt(100), and Pt(110) single-crystal electrodes and of a spherical, monocrystalline, polyoriented Pt electrode [Pt(spherical)] in aqueous 10 M NaOH solution during cathodic corrosion. We examine the changes in the surface morphology of the Pt electrodes as a function of cathodic corrosion potential and the corrosion time by using cyclic voltammetry (CV), scanning electron microscope (SEM), and atomic force microscopy (AFM). The CV analysis reveals the onset of cathodic corrosion and the evolution of atomic-scale structural transformation from an electrochemical perspective. Complementing these insights, the SEM and AFM images show the evolution of surface morphologies and patterns in these monocrystalline electrodes. Our study confirms that the cathodic corrosion on monocrystalline electrodes takes place at potentials $E_p \sim< -0.5$ V vs. reversible hydrogen electrode (RHE) and leads to the creation of (100) step and terrace sites and the destruction of (110) step-like features (10). During the initial stages of cathodic corrosion, the Pt(100) surface develops square pits, the Pt(111) surface develops triangular pits, and the Pt(110) surface develops rectangular pits. Remarkably, cathodic corrosion appears the most detrimental for Pt(111) and the least for Pt(110). Upon longer-term corrosion, the distinct pit shapes grow, overlap, and transform into a self-similar fractal-type etching pattern. The shape of the etch pit is determined by the fact that cathodic corrosion occurs predominantly in the <111> direction.

Results

Corrosion Initiation. Fig. 1 *A–D* present a series of the hydrogen desorption region of a series of CV profiles for the Pt(100), Pt(111), Pt(110), and Pt(spherical) electrodes, respectively, in 0.1 M H_2SO_4 after cathodic corrosion at different polarization potentials E_p (-0.5 9 E_p 9 -1.0 V) for a constant polarization time (t_p = 60 s). Due to the symmetrical nature of anodic and

Significance

Cathodic corrosion is a relatively unexplored but highly enigmatic electrochemical phenomenon that transforms, roughens, and dissolves metal surfaces under cathodic polarization. We show how cathodic corrosion of a platinum spherical single-crystal electrode in an aqueous alkaline electrolyte leads initially to the formation of etch pits that reflect the local symmetry of the surface and subsequently develop into a growth regime in which self-similar diffusion-limited patterns emerge. These are unique observations that may eventually open the door to controlled surface patterning and nanoparticle preparation.

Author contributions: N.A., T.J.P.H., and M.T.M.K. designed research; N.A. performed research; N.A., T.J.P.H., and M.T.M.K. analyzed data; and N.A., T.J.P.H., and M.T.M.K. wrote the paper.

The authors declare no competing interest.

This article is a PNAS Direct Submission.

[1]Present address: Stanford Synchrotron Radiation Lightsource, SLAC National Accelerator Laboratory, Menlo Park, CA 94025.

[2]To whom correspondence may be addressed. Email: m.koper@chem.leidenuniv.nl.

This article contains supporting information online at https://www.pnas.org/lookup/suppl/doi:10.1073/pnas.2017086117/-/DCSupplemental.

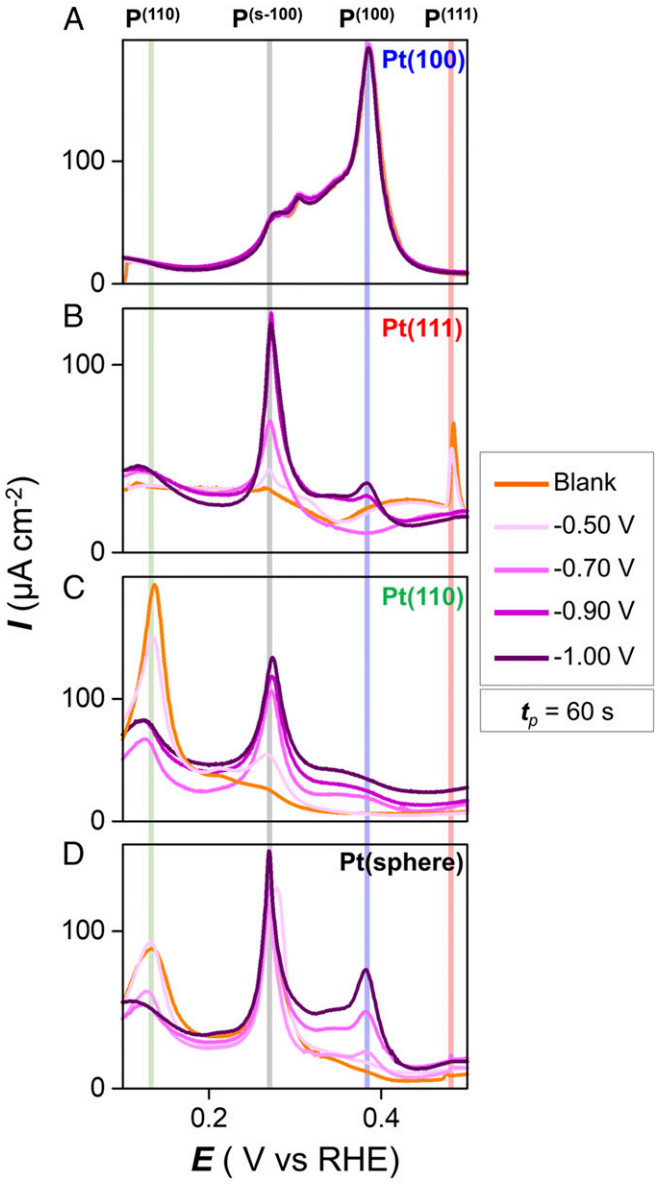

Fig. 1. Modification of hydrogen desorption region of the CV profiles in 0.1 M H_2SO_4 solution after cathodic corrosion in 10 M NaOH at the indicated polarization potentials for 60 s. CV profiles for the (*A*) Pt(100), (*B*) Pt(111), (*C*) Pt(110), and (*D*) Pt(spherical) electrodes in the 0.05 V $\leq E \leq$ 0.60 V range acquired immediately after the cathodic corrosion treatment. The orange CV profile refers to the given electrode before the cathodic corrosion. The subsequent three CV profiles (light pink to dark pink) refer to E_p = −0.5, −0.7, −0.9, and −1.0 V. Each CV profile corresponds to a freshly prepared monocrystalline electrode surface. Scan rate is 50 mV s^{-1}.

cathodic scans of the hydrogen region, we show in Fig. 1 only the anodic part of the full CV. The entire CV profiles including the hydrogen adsorption and desorption regions are included in *SI Appendix*, Fig. S1. Each CV profile corresponds to an independent experiment performed using a freshly prepared monocrystalline electrode. The CV profiles before cathodic polarization are color-coded as orange. The current density of the CV profiles is calculated based on the geometric surface area. For all four electrodes, the corrosion onset potential is (close to) −0.5 V vs. RHE (in 10 M NaOH) as concluded from the observation that CV profiles of electrodes treated at potentials less negative than −0.5 V vs. RHE (−0.1, −0.2, −0.3, and −0.4 V) reveal no modification. This onset potential is in agreement with the earlier established onset potential for −0.4 V vs. RHE for polycrystalline Pt electrodes in 10 M NaOH (11). The exact corrosion onset potential can vary mildly based on iR compensation and other factors (14); also note that our procedure for determining the onset potential does not have an accuracy better than 0.1 V. The CV profiles shown in Fig. 1 are color-coded with the light pink curve representing the CV profile for E_p = −0.5 V vs. RHE and the dark red representing the CV profile for E_p = −1.0 V vs. RHE. In agreement with earlier results for polycrystalline Pt electrodes, the CV profiles of all four electrodes show that cathodic polarization leads to the preferential formation of (100)-type sites (11).

In the case of Pt(100) (Fig. 1*A*) and $E_p \leq$ −0.5 V, the CV profiles undergo minor changes. The intensity of the principal peak at 0.37 V, P^{100}, attributed to long-range ordered (100) terraces (24, 25), stays the same while the intensity of peak at 0.27 V (P^{s-100}, attributed to (100)-type steps (24, 25), shows a minor increase. These observations indicate that only relatively few new sites are created in the Pt(100) electrode upon cathodic corrosion.

In contrast, Pt(111) (Fig. 1*B*) suffers a significant modification. The intensity of the initial sharp peak at 0.47 V (P^{111}), which is assigned to (bi)sulfate adsorption on long-ranged ordered (111) terraces (24, 25), decreases; this feature practically vanishes in the case of $E_p \leq$ −0.7 V. The intensities of the two peaks at 0.37 and 0.27 V, which are attributed to (100)-terrace and (100)-step–type sites (24, 25), both increase as E_p is extended toward more negative values. These observations point to the significant structural transformation of the initially (111) surface to a (disordered) surface with newly developed (100)-type sites.

In the case of Pt(110) (Fig. 1*C*), the orange CV profile (before cathodic corrosion) refers to the reconstructed Pt(110) electrode obtained upon annealing and cooling in H_2/Ar atmosphere (26). The CV profile of Pt(110) undergoes significant changes for corrosion potentials more negative than −0.5 V. The intensity of the initial sharp peak at 0.13 V (P^{110}), which is attributed to long-range ordered (110)–(1 × 2) terraces (26), decreases in height as E_p is made more negative. This decrease in (110) steps is accompanied by an increase in (100) terraces and (100)-oriented steps. These observations suggest that cathodic corrosion of the initial (110) surface leads to a surface composed of many structural defects having the (100) orientation, most likely in the form of small terraces and steps.

Finally, we studied the cathodic corrosion of the Pt (spherical) electrode (Fig. 1*D*), comprising low Miller index facets having the (111), (100), and (110) orientation, as well as stepped and kinked facets with higher Miller indices. For the spherical electrode, cathodic treatment at progressively negative voltages below −0.5 V leads to 1) the development of (100) terrace and step sites, 2) the suppression of (110) step sites and (111) terrace sites, and 3) the increasing amount of (100) step sites. In summary, cathodic corrosion leads to an enhancement of (100) step and terrace sites and the destruction of (111) terrace and (110) step-like features for all four electrodes shown in Fig. 1.

To visualize the morphological changes due to cathodic corrosion, we captured SEM and AFM images of the corroded Pt(spherical) electrodes and the cut single-crystal electrodes. Fig. 2 presents SEM images of the Pt(spherical) electrodes (second to the fourth column), AFM images (fifth column), and single-crystal Pt basal surfaces [sixth column; Pt(100), Pt(111), and Pt(110)] after cathodic corrosion at the polarization potential of −1.0 V for 60 s. The three rows show the corroded Pt(spherical) and single-crystal electrode in the different basal plane orientation, namely, (100), (111), and (110) facets.

For these rows, the first and the second columns display the model 3D spherical FCC crystal and the SEM images of the corroded spherical Pt crystal in three different basal plane orientations, to emphasize the overall corrosion behavior along

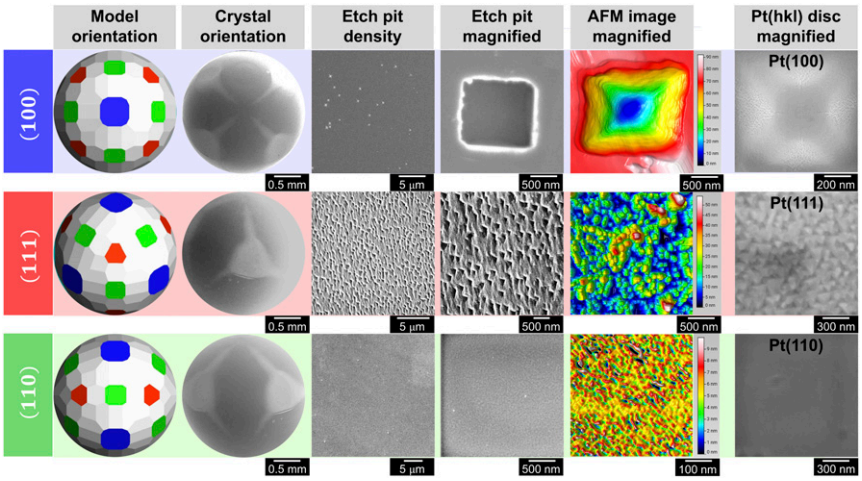

Fig. 2. Surface roughness development on Pt single crystals during cathodic corrosion at the polarization potential E_p of −1.0 V in 10 M NaOH electrolyte for 60 s, as observed by SEM and AFM. The first and the second columns show the model and actual spherical single crystal in (100), (111), and (110) orientations. A lighter color in the second column signifies a more roughened surface due to so-called edge effects (27). The third and fourth columns show the overview and the magnified SEM images of the etch pattern in the (111), (100), and (110) facets of the corroded spherical single crystal. The fifth column shows AFM images to show the roughness development on the (111), (100), and (110) facets. The SEM images (fourth column) and AFM images (fifth column) are not measured at identical locations. The sixth column shows the surface morphology developed for the Pt(100), Pt(111), and Pt(110) disk electrodes.

various zones. The images in the second column emphasize that the stepped surfaces along the (100) to (111) zone are more roughened in comparison to the stepped surfaces along (100) to (110) and (110) to (111) zones. The third column reveals the (visible) pit density of basal plane facets of Pt(spherical) electrode in which (111) facets have most pits while the (110) facets contain no visible pits. The fourth column shows further zoomed-in SEM images of the three facets to highlight the shape of the pits. The fifth column shows corresponding AFM images of the three facets to highlight the shape of the pits. The SEM images (fourth column) and AFM images (fifth column) are not measured at identical locations.

In Fig. 2, the (100) facet reveals a square-shaped pit, and the (111) facet reveals a triangular pit, while the (110) facet shows no visible pits for the given magnification. However, as we will show below, longer corrosion times reveal a rectangular pit shape on Pt(110).

For comparison with these pit shapes on the spherical single crystal, the fifth column in Fig. 2 displays the pit shapes of cut basal plane single crystals. As expected (11), the (100) facet reveals a square-shaped frustum pit (evolved from the square pit), and the (111) facet reveals a triangular pit, while the (110) facet shows no visible pits for the given magnification. Interestingly, as we suggested in previous work (11), the pit density and shape are different for the three low Miller index facets, and their morphology is uniquely related to the initial orientation of the surface.

From Figs. 1 and 2, we conclude that the initial cathodic corrosion of platinum is structure-sensitive, manifested by differently shaped etch pits on the three low-index planes. The etch pits enhance the (100) morphology (both terraces and steps) of the surface, which leads to square etch pits on Pt(100) and triangular etch pits on Pt(111). We note that according to the SEM images, the cathodic corrosion of the Pt(110) appears slower than the other two surfaces; visible rectangular pits are seen only after longer corrosion times, as will be shown below in the section *Evolution of Cathodic Corrosion*. However, the evolution of the Pt(110) CV profile in Fig. 1 shows that surface modification as a result of cathodic corrosion clearly takes place; the conclusion must be that these modifications have a length scale that is not visible with SEM. Cathodic corrosion appears fastest on Pt(111), in agreement with the CV observations in Fig. 1.

Evolution of Cathodic Corrosion. In order to understand the temporal evolution of the surface as a result of cathodic corrosion, Pt(111), Pt(110), Pt(100), and Pt(spherical) electrodes were subjected to cathodic treatment at a constant polarization potential ($E_p = -1.0$ V) for six different polarization times t_p, (t_p = 1, 5, 10, 15, 20, and 25 min) in a 10 M NaOH solution. As mentioned in the experimental section, all experiments on both spherical and basal plane electrodes were conducted with a freshly prepared electrode and electrolyte. As before, a CV profile was measured in 0.1 M H_2SO_4 solution after cathodic treatment to determine electrochemically if any modification in the surface structure had occurred. Furthermore, we acquired SEM and AFM images of the corroded Pt(spherical) and basal plane electrodes to follow the evolution of surface morphology and the development of surface pits (surface pattern formation) as a function of polarization time.

Fig. 3 shows the electrochemical results of the progression of cathodic corrosion. Fig. 3*A* shows the current–time profile of Pt(spherical) electrode during cathodic corrosion at the polarization potential E_p of −1.0 V in 10 M NaOH electrolyte for

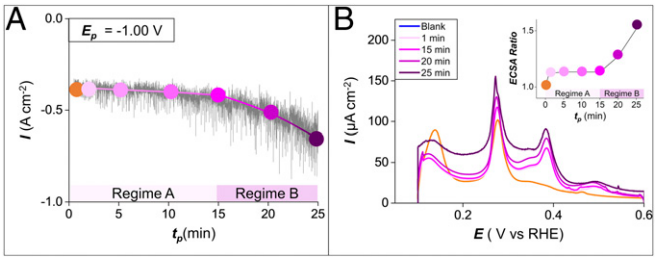

Fig. 3. Progression of cathodic corrosion and its corresponding structural transformation as detected in the CV profile. (*A*) Chronoamperometry profile of Pt(spherical) electrode during cathodic corrosion at the polarization potential E_p of −1.0 V in 10 M NaOH electrolyte for 25 min. (*B*) Modification of hydrogen desorption region of the CV profile in 0.1 M H_2SO_4 solution after cathodic corrosion at the polarization potential E_p of −1.0 V in 10 M NaOH electrolyte for various polarization times. Each CV profile corresponds to a freshly prepared monocrystalline electrode surface. The scan rate is 50 mV s^{-1}. (*Inset*) The ECSA ratio, calculated from the CV profiles, as a function of the polarization time.

25 min. The current–time profiles of the other five measurements (t_p = 1, 5, 10, 15, and 20 min) for the Pt(spherical) electrode are excluded as their profiles superimpose to t_p = 25 min. Fig. 3*A* shows that the corrosion progresses in two stages, as color-coded by the light pink and dark pink regimes. During initial corrosion (regime A), until ca. 15 min under the conditions of this specific experiment, the cathodic current is nearly constant. This cathodic current is due to the evolution of hydrogen on the platinum surface. After ca. 15 min, the current starts to increase more drastically (regime B). The increase in the current can be attributed to an increase in the electrochemical surface area (Fig. 3*B*, *Inset*), which will be corroborated using hydrogen desorption CV profile in Fig. 3*B*.

Fig. 3*B* shows the modification of hydrogen desorption region of the CV profile in 0.1 M H_2SO_4 solution after cathodic corrosion at the polarization potential E_p of −1.0 V in 10 M NaOH electrolyte for various polarization times. The entire CV profiles including the hydrogen adsorption and desorption regions are included in *SI Appendix*, Fig. S1. After the cathodic treatment, the shape of the CV profile does not change for t_p between 1 and 15 min (light pink curves and light pink region in Fig. 3*B*). The stability of the CV profiles suggests that the overall modification of surface roughness and the relative surface specificity stays the same. This voltammetric overlap below 15 min matches earlier preliminary results on Pt wire electrodes (14). However, for longer cathodic corrosion times of >15 min (the dark pink region in Fig. 3*B*), the CV profiles show the development of a higher surface area without changes in individual CV features. In this longer-time corrosion regime, the increase in the surface area without changes in the specific CV features suggests that the relative ratios of individual facets on the surface of corroded Pt(spherical) remain constant, but their respective sizes increase. Fig. 3*B*, *Inset*, shows the relative roughness factor (ratio of the electrochemical surface area [ECSA] of the electrode after and before corrosion) as a function of time. Similar to Fig. 3 *A* and *B*, the roughness factor is constant until 15 min (red region) but drastically increases after 15 min.

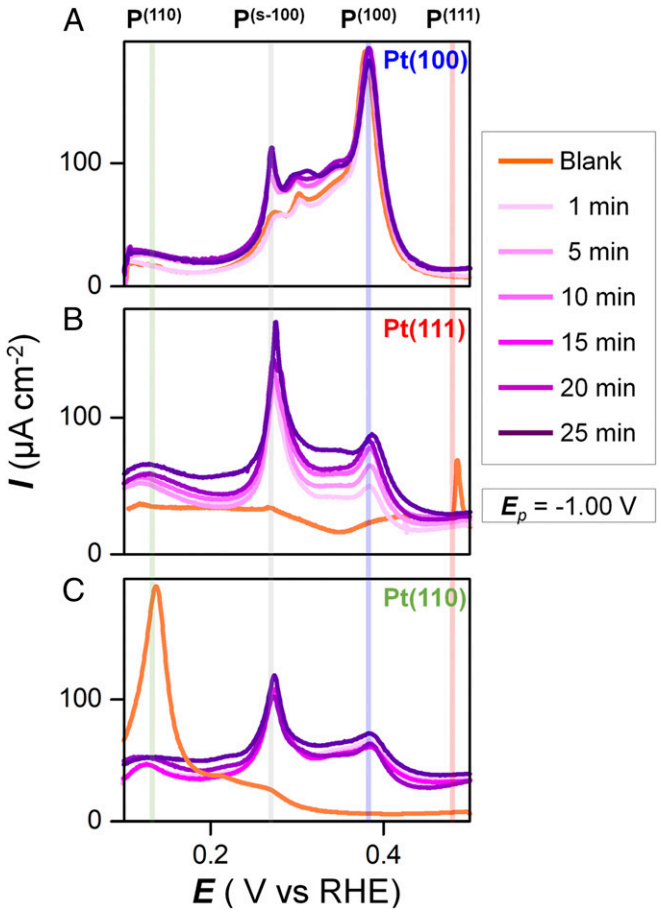

Fig. 4. Modification of hydrogen desorption region of the CV profiles in 0.1 M H_2SO_4 solution after cathodic corrosion in 10 M NaOH at the constant polarization potentials for the indicated polarization time. CV profiles for (*A*) Pt(100), (*B*) Pt(111), and (*C*) Pt(110) in the 0.05V ≤ *E* ≤ 0.60 V range acquired immediately after the cathodic corrosion treatment. The orange CV profile refers to the given electrode before the cathodic corrosion. The subsequent six CV profiles (light pink to dark pink) refer to t_p = 1, 5, 10, 15, 20, and 25 min. Each CV profile corresponds to a freshly prepared monocrystalline electrode surface. Scan is rate 50 mV s^{-1}.

Fig. 4 *A*–*C* present a series of hydrogen desorption region of the CV profiles for the Pt(100), Pt(111), and Pt(110) electrodes, respectively, in 0.10 M aqueous H_2SO_4 after cathodic corrosion at different polarization times, for a constant polarization potential (E_p = 1.0 V) [Fig. 3B shows the same profiles for the Pt(spherical) electrode]. The entire CV profiles including the hydrogen adsorption and desorption regions are included in *SI Appendix*, Fig. S2. In the case of Pt(100) (Fig. 4*A*), the intensity of the principal peak at 0.37 V (P^{100}) attributed to long-range ordered (100) terraces stays the same while the intensity of peak at 0.27 V (P^{s-100}) corresponding to stepped Pt(100) shows a significant increase. These observations indicate that stepped Pt(100) sites are created in the Pt(100) electrode due to cathodic corrosion. Additionally, there is a minor change in the overall electrochemical surface area change.

In the case of Pt(111) (Fig. 4*B*), the intensity of the initial sharp peak at 0.47 V (P^{111}), which is assigned to (bi)sulfate adsorption on long-ranged ordered (111) terraces, vanishes, and intensity of the two peaks at 0.37 and 0.27 V, which are attributed to (100) terrace and (100) step-type sites, both increase. Importantly, the electrochemical surface area gradually increases with time. These observations point to the significant structural transformation of the initial (111) surface to a (disordered) surface with newly developed (100)-type sites and its defect density rapidly increasing with time.

In the case of Pt(110) (Fig. 4*C*), the orange CV profile (before cathodic corrosion) refers to the reconstructed Pt(110) electrode obtained upon annealing and cooling in H_2/Ar atmosphere. The intensity of the initial sharp peak at 0.13 V (P^{110}) attributed to long-range ordered (110)-(1 × 2) terraces vanishes within the first minute, and the intensities of the two other features, a broader wave at 0.37 V and a peak at 0.27 V, which are ascribed to (100) terraces and (100)-oriented steps, respectively, are developed within the first minute and increase slowly afterward. In general, for the Pt(110), only mild modification of the CV profile and the electrochemical surface area occurs after the first minute. These observations suggest that cathodic corrosion of the initial (110) surface quickly leads to a surface composed of structural defects having the (100) orientation, after which its defect density slowly increases with time.

Fig. 5 presents SEM images of the Pt(spherical) electrode after 1, 5, 10, 15, 20, and 25 min at a polarization potential E_p of −1.0 V. SEM imaging of the Pt(spherical) electrode for increasing polarization times demonstrates the continuous development of corrosion pits. More importantly, the SEM images show different surface morphologies in the two stages found in the electrochemical experiments in Fig. 3 (color-coded by light pink and dark pink). The short-time corrosion (light pink region), shown in Fig. 5 by the corroded surfaces with t_p of 1, 5, and 10 min, reveals a faceted type etching with individual etch pits [note the rectangular etch pit on the (110) facet]. However, the longer-time corrosion (light pink region), shown in Fig. 5 by the

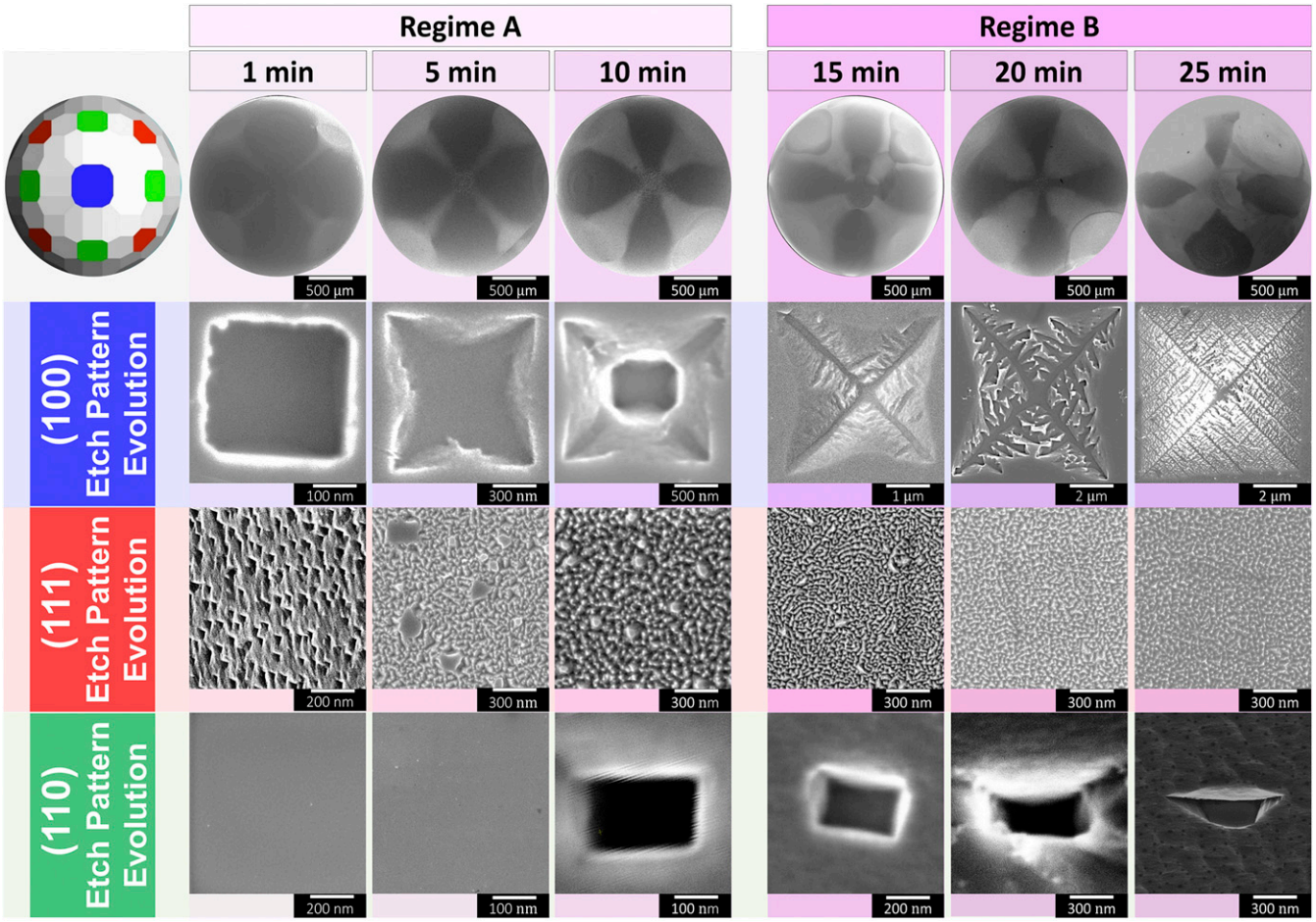

Fig. 5. Evolution of surface morphology upon cathodic corrosion at various polarization times at $E_p = -1.0$ V, as illustrated by SEM images of the Pt(spherical) electrode after 1, 5, 10, 15, 20, and 25 min. The first row shows SEM images of the entire Pt(spherical) electrode; the other rows show the SEM images of the (111), (100), and (110) facets.

corroded surfaces with t_p of 15, 20, and 25 min, reveals a more self-similar fractal-type etching, specifically for the (100) facet.

The micrographs in the first row of Fig. 5 emphasize that the stepped surfaces along the (100) to (111) zone are more roughened in comparison to the stepped surfaces along the (100) to (110) and (110) to (111) zones, as the surface appears lighter in the (100) to (111) zone. Also, the roughening width along the (100) to (111) zone increases with time while the roughening along the (100) to (110) zone shows only minor changes. In the case of basal plane etching (second to the fourth row), the pit size, the pit density, and the apparent roughness (as judged from the grayscale of the image) grow with time.

Furthermore, the morphology of the pits, especially the (100) pit, can be divided into two regimes. The second row shows the evolution of Pt(100) etch pit pattern. Initially (regime A), the etch pit sides appear smooth and faceted, but at a later time (regime B), the pits roughen in a self-similar fashion. In the initial stage of corrosion (regime A), the square pit slowly transforms into a pyramidal pit, while upon a longer period (regime B), the pyramidal pit develops self-similar side arms. The third row shows the evolution of Pt(111) etch pit pattern. Initially, Pt(111) forms a triangular pit with the pit density increasing over time; at longer times, the pits overlap, and the surface becomes rougher. The final row shows the evolution of Pt(110) etch pit pattern. The pit shape is initially rectangular and becomes more wedge-shaped over time.

To further analyze the exact shape of the pit developing in the Pt(100) facet, we performed AFM imaging (Fig. 6). Fig. 6 shows the 3D AFM images with stereographic projection (alongside the corresponding SEM image) and the etching profile along with crystallographic directions for the (100) pits generated after 5 and 25 min of corrosion. The (100) pits generated after 5 and 25 min of corrosion were chosen here in order to compare the two regimes of corrosion. First, what looks like a square pit in the SEM image [(100) row of Fig. 5] appears more like a concave equilateral octagon pit in the AFM images. The concave nature of the pit wall is clearly visible in the etch profile along with the different crystallographic directions (Fig. 6). Interestingly, the depth (z axis) of both pits is approximately constant (100 nm) while the lateral size of the pit increases 10-fold by going from 5 to 25 min of etching. Second, the material removal is maximum in the direction of (111) and the least in the direction of (110). This observation is consistent with the previous conclusion that the (111) facet corrodes the fastest, while the (110) facet corrodes the slowest. The bottom row (25 min) shows a pit with a fractal-type etching, for which we find that the profile roughness is highest in the case of the (110) direction and lowest in the (111) direction.

From the information obtained from AFM and SEM data, one can model the temporal shape evolution of the (100) pit. Fig. 7 shows the progression of the (100) pit shape in the two regimes. Fig. 7*A* shows the progression of faceted etch pits, while Fig. 7*B* shows the progression of fractal-type etch pits. Fig. 7 *A* and *B*

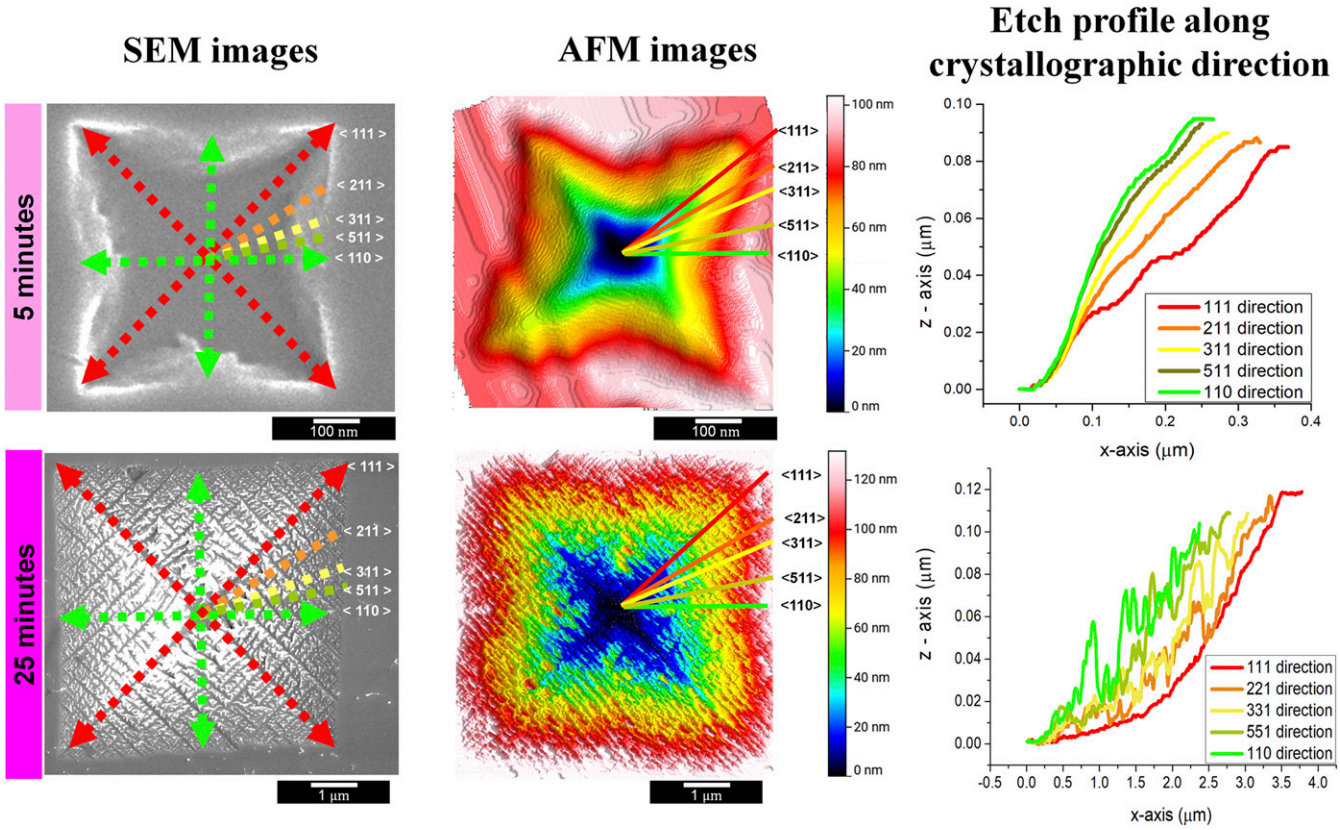

Fig. 6. Analysis of the (100) pit shape in regimes A and B (Fig. 5). (*Left*) The SEM image of the (100) pit, indicating the stereographic projection. (*Middle*) The AFM images of the (100) pit. (*Right*) The AFM profile along with specific crystallographic directions. The (100) pit after (*Top*) 5 and (*Bottom*) 25 min.

have two rows each where the top row shows the actual SEM images and the bottom row shows the modeled pit. During faceted etching, the pit starts as a cubic pit with etching accelerating in the (111) direction (i.e., along with the four corners of the cubic pit). Over time, the progressive etching in the (111) direction transforms the cubic pit into a concave equilateral octagon pit. After 15 min, side arms develop along with the four (111) directions, and a fractal-type pattern emerges, resembling a pattern generated by diffusion-limited aggregation or annihilation (28).

Cathodic Corrosion of High-Index Surfaces. To further analyze the anisotropic etching concerning the initial surface arrangement of atoms, we generated a library of SEM images along with the stereographic triangle. Fig. 8 presents SEM images of etched high-index surfaces along the (100) to (110) direction. The figure has three rows where the top row shows the stereographic projection of the etching direction of each facet and the second and third row show the actual SEM images of faceted-type and fractal-type etching. It contains six columns where the first column shows the entire etched spherical crystal, while the others contain SEM images of low Miller index facets (shown in the second and last column) and three high-index facets along the (100) to (110) direction.

It is observed that 1) the etching is dominant along the (111) direction in both low- and high-index planes; 2) the etching is two-staged i.e., initially it start as a faceted etching and over time it transforms to fractal etching; and 3) the size and density of the pit gradually reduce when moving from the (100) facet to the (110) facet.

Fig. 9 presents SEM images of etched high-index surfaces along the (100) to (111) direction. The figure has three rows where the top row shows the stereographic projection of etching direction of each facet and the second and third row show the actual SEM images of faceted-type and fractal-type etching. It contains six columns, where the first column shows the entire etched spherical crystal and the others contain SEM images of low Miller index facets (shown in the second and last columns) and three high-index facets along the (100) to (111) direction. The analysis of the images leads to the following observations: 1) the etching is dominant in the (111) direction in both low- and high-index planes; 2) the etching is two-staged, i.e., initially, it starts as a faceted etching, and over time it transforms into fractal etching; and 3) the size of the pit is reduced while the density of the pits gradually increases when going from (100) to (111).

Finally, Fig. 10 presents SEM images of etched high-index surfaces along the (110) to (111) direction. Since the (100) facet or direction is not included along this side of the stereographic triangle, the etch patterns are less dramatic than in Figs. 8 and 9. No fractal branched patterns as observed for the vicinal (100) surface are observed in Fig. 10, because the corrosion rate on the (110) facet is too low.

Discussion

The results shown in the previous section have illustrated the fascinating and intricate patterns that develop on a single-crystalline platinum electrode under conditions of cathodic corrosion. While it is not the purpose of this paper to develop a detailed model for how these etch patterns form, we do want to provide a brief discussion of possible mechanisms involved in the process of cathodic corrosion and the corresponding pattern formation.

Although the chemistry involved in cathodic corrosion is still not fully understood, we have previously suggested that cathodic

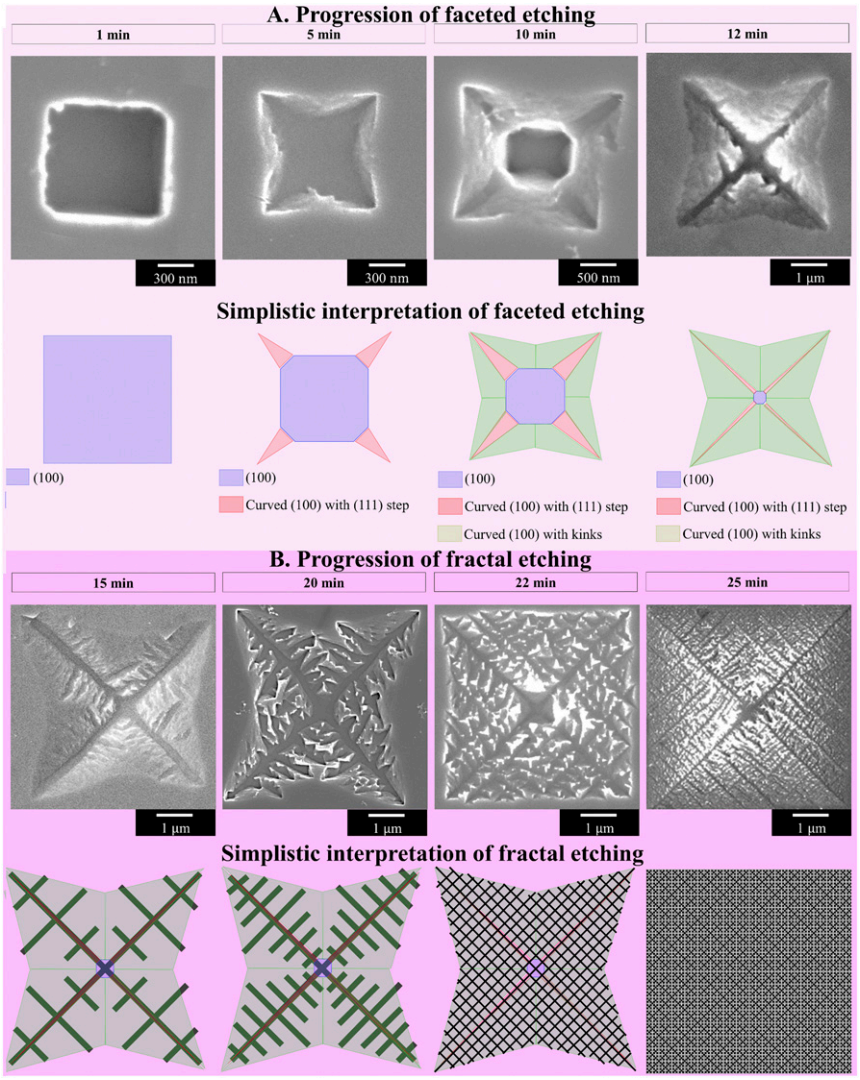

Fig. 7. Two-staged temporal evolution of a (100) pit shape with SEM images with a simplified interpretation of their growth development, for illustrative purposes. (*A*) The progression of faceted etching and (*B*) the evolution of fractal etching.

corrosion of platinum is initiated by the formation of ternary metal hydride phases (14). The stability of these phases depends on the interaction with the electrolyte cation and the adsorption of hydrogen on platinum. We hypothesize that these ternary metal hydride phases are the (chemical) intermediate in the observed pattern formation and the roughening of the platinum electrode. As described, the cathodic etching appears to take place in several stages. In the initial stage, single etch pits are formed on the surface, presumably at defects and step edges (11), and their shape is dictated by the single-crystalline facet on which the corrosion takes place. This process is the fastest on Pt(111), yielding triangular pits, and slower on Pt(100), yielding square pits. The Pt(110)-(1 × 2) surface is quickly transformed in the initial phase of cathodic corrosion but then corrodes much slower, eventually yielding visible rectangular pits. In the SEM, the roughening of the Pt(110) surface is hardly visible.

In the second stage of cathodic corrosion, the regular etch pit shape becomes unstable and starts corroding preferentially in the (111) direction, although we note that we only see this explicitly for the facets close to the (100) zone. This leads to four arms developing in the etch pit, yielding a concave octagon-shaped pit. In the next stage of corrosion, these arms develop side arms, yielding a branched pattern very similar to a diffusion-limited aggregate (DLA) (28). While classical DLA patterns are random, the patterns observed during cathodic corrosion clearly have a preferred directionality, and therefore, they have a very high degree of anisotropy. The observed patterns strongly suggest the importance of surface mass transport (or any other Laplacian process) in their generation (28, 29). On the (111) facet, we have not observed DLA-type patterns, perhaps because the pit density is much higher on this surface, and pits start overlapping much faster than on the (100) surface, or perhaps because the resolution of the SEM images is simply not high enough. DLA-type patterns have been previously observed in a variety of (electrochemical) growth processes (28). Similar DLA-type etching patterns have been observed during the chemical etching of graphene (30) and the photoelectrochemical etching of n-silicon (31).

Finally, we note that it is challenging to follow the development of these etch structures in situ during the electrochemical process. During cathodic corrosion, large amounts of hydrogen are evolved, strongly hampering atomic-scale interrogation and imaging of the platinum surface. Future work will definitely need

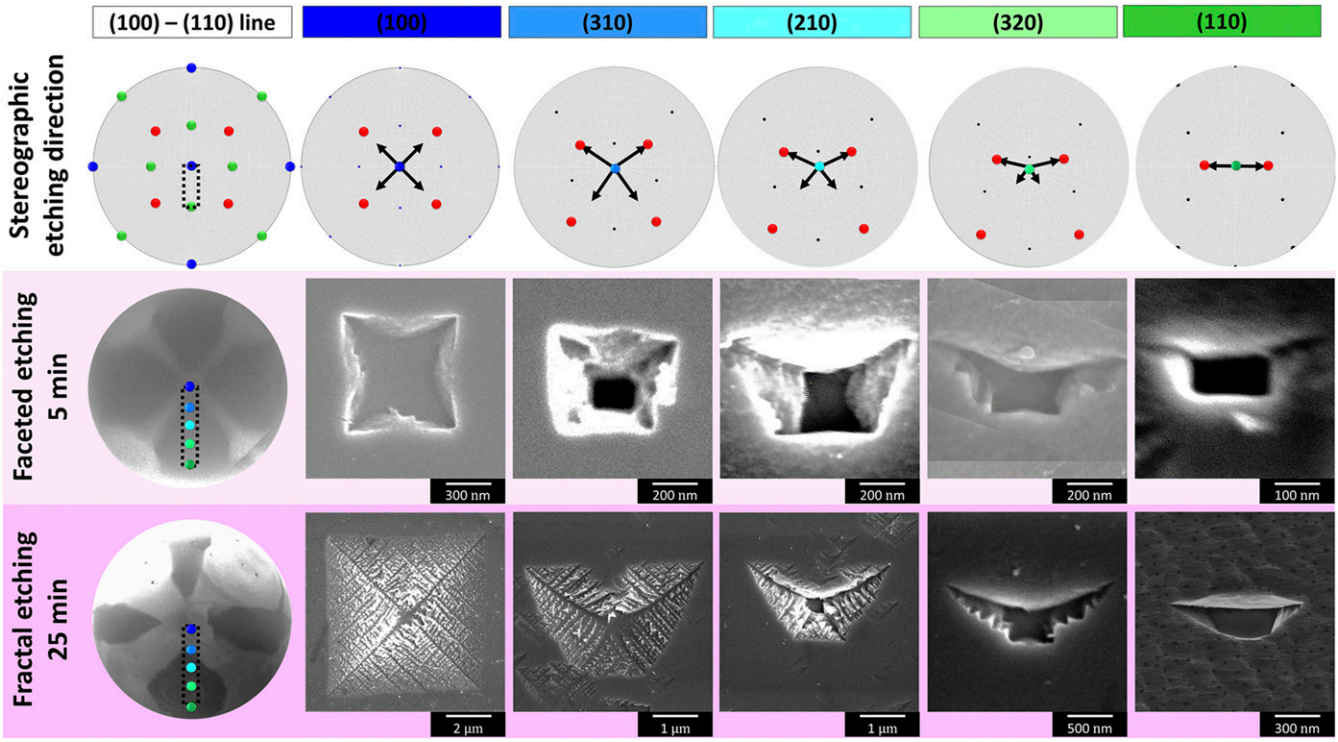

Fig. 8. Etching patterns observed along the 100 to 110 stereographic direction. (*Top*) The stereographic etching direction and SEM images of (*Middle*) faceted and (*Bottom*) fractal etching. The red dot represents the (111) direction, blue dot represents (100), and green represents (110). Arrows show preferred etch directions.

to address this issue, especially if we want to employ cathodic corrosion as a nanostructuring tool.

Conclusion

In this paper, we have employed a spherical single crystal of platinum to study the facet dependence of an enigmatic electrochemical phenomenon, i.e., cathodic corrosion. Our study has revealed that the anisotropic corrosion of the platinum electrode takes place in different stages. Initially, etch pits are formed which reflect the local symmetry of the surface: square pits on (100) facets, triangular pits on (111) facets, and rectangular pits on (110) facets. Following previous work, we hypothesize that these etch pits are formed through a ternary metal hydride corrosion intermediate (14). Intriguingly, the (111) facet corrodes the fastest, and the (110) facet corrodes the slowest, in contrast to the facet dependence known for anodic corrosion (21). For corrosion on the (100) facet and on higher-index surfaces close to the (100) plane, the etch pit destabilizes in a second growth stage, by etching faster in the (111) direction, leading to arms in the etch pit, yielding a concave octagon-shaped pit. In a third growth stage, these arms develop side arms, leading to a structure that strongly resembles a self-similar diffusion-limited growth pattern, with strongly preferred growth directions.

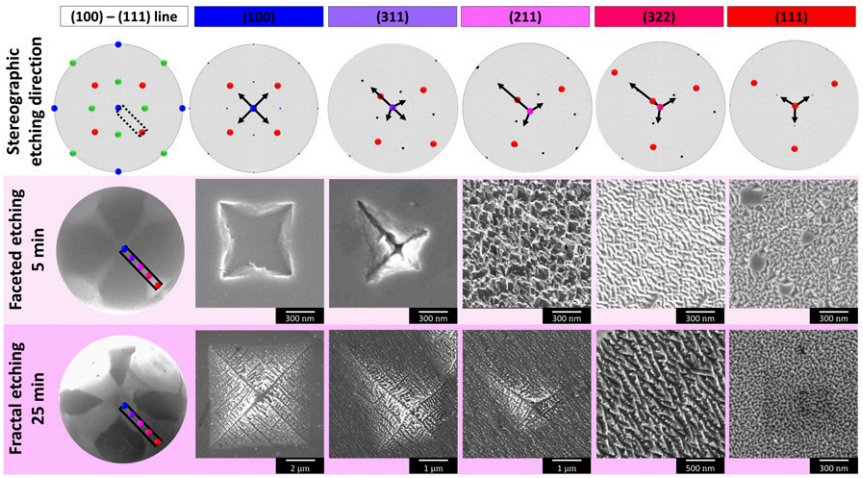

Fig. 9. Stereographic etching direction and SEM images of etched pits along the 100 to 111 line. (*Top*) The stereographic etching direction and (*Middle* and *Bottom*) SEM images. The red dot represents the (111) direction, blue dot represents (100), and green represents (110). Arrows show preferred etch directions.

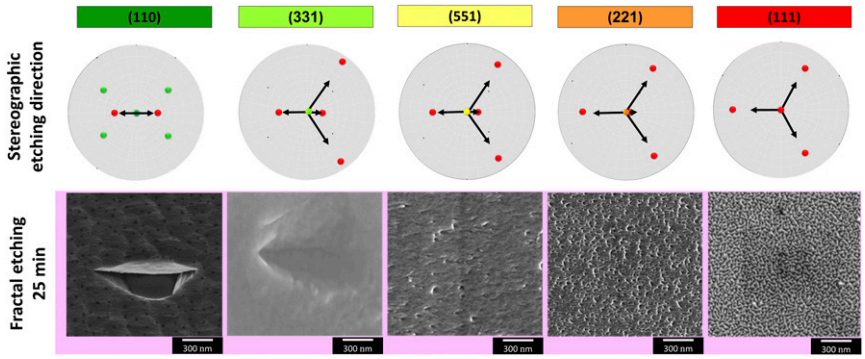

Fig. 10. Stereographic etching direction and SEM images of the etched pit along the 101 to 111 line. (*Top*) The stereographic etching direction and (*Bottom*) SEM images. The red dot represents the (111) direction. Arrows show preferred etch directions.

The unique observations illustrated in this paper reflect a largely unexplored branch of chemistry of metal surfaces in aqueous solutions that allows one to pattern surfaces and synthesize nanoparticles. Much more future work will need to be done to understand the chemistry and the growth dynamics behind this phenomenon, including in situ studies of the chemical intermediates involved and a higher-resolution mapping and understanding of the roughness development and the associated pattern formation. Also, it will be important to investigate the generality of the phenomenon in relation to other metals. Preliminary work on gold electrodes shows that cathodic corrosion on gold is also highly anisotropic but leads to very different surface structures developing during the corrosion (14).

Materials and Methods

Electrodes, Electrolytes, and Electrochemical Cells. Two types of custom-made electrochemical cells were employed in this study, namely, a Pyrex glass cell and a fluorinated ethylene propylene (FEP) cell. The two-compartment Pyrex glass cell was used in all CV measurements in acid media, and the FEP cell was employed in cathodic corrosion measurements in alkaline media. The H_2SO_4 (ultrapur, Merck) and NaOH (suprapur, Merck) electrolyte solutions were prepared using ultrahigh-purity (UHP) water (Milli-Q, Millipore; resistivity $\geq$ 18.2 MΩ cm). The glassware was cleaned using well-established standard procedures (32). UHP Ar (Linde, HiQ 6.0) was passed through and above the electrolyte to remove any dissolved gases. A platinum mesh (5N purity) was used as a counter electrode, and an RHE (HydroFlex, Gaskatel) was used as a reference electrode. The use of a platinum counter electrode did not affect the observations. The same observations were made using a titanium-based dimensionally stable anode as the counter electrode. We also note that during cathodic corrosion of the working electrode, the potential at the counter electrode was ca. 2.0 V and constant. As Cherevko et al. have shown (33), platinum dissolution happens primarily during dynamic operation of the platinum electrode and especially during the reduction of the Pt oxide.

The monocrystalline Pt(111), Pt(110), Pt(100), and Pt(spherical) [together referred as Pt(*hkl*)] working electrodes are prepared using the flame fusion method (34). Details of the procedures employed in their orientation, cutting, polishing, and final thermal treatment have been explained elsewhere (35). Prior to each measurement, the spherical single crystal is entirely regrown while cut crystals [Pt(111), Pt(100), and Pt(110)] are annealed at 1,100 °C in Ar/H_2 atmosphere for at least 30 min in an induction annealing system (32). After annealing the monocrystalline Pt electrodes, they were cooled in a controlled atmosphere [Ar/H_2 mixture (3:1 ratio)], protected by a droplet of UHP water, and subsequently transferred to the electrochemical cell. In this cell, the so-called hanging meniscus electrode–electrolyte connection was established between the Pt(111), Pt(110), or Pt(100) electrodes and the electrolyte. In the case of Pt(spherical), the electrode was carefully placed in the electrolyte so that the monocrystalline Pt sphere was entirely submerged, and the stem wire was above the electrolyte surface (32). All electrochemical experiments were conducted using a Bio-Logic SP-300 potentiostat.

Cathodic Corrosion Studies. The first set of experiments was designed to determine the onset potential of cathodic corrosion. Here Pt(*hkl*) electrodes were subjected to potentiostatic cathodic polarization (CA), starting from an initial potential of E_p= 0.0 V, and extended toward more negative values (with interval of - 0.1 V) up to $E_p = -1.0$ V for a constant polarization time (t_p = 60 s) in a 10 M NaOH solution. Before and after cathodic polarization, the electrodes were subjected to CV measurements in the 0.1 M H_2SO_4 solution to verify their characteristic hydrogen underpotential adsorption/desorption profile to determine if any modification in the surface structure had occurred. The second set of experiments was designed to understand the evolution of surface morphologies during cathodic corrosion. Here, Pt(*hkl*) electrodes were subjected to cathodic treatment at a constant polarization potential ($E_p = -1.0$ V) for six different polarization times t_p (t_p = 1, 5, 10, 15, 20, and 25 min) in a 10 M NaOH solution. For both sets of experiments, each measurement was conducted using a freshly prepared electrolyte and electrochemical cell to avoid carryover of dissolved platinum ions and other contaminations.

Fig. 11 displays a potential versus time profile that illustrates the sequence of steps (a through e) involved in the corrosion studies.

Step a is acquisition of a CV profile in the $0.07\ V \leq E \leq 0.50$ V range in 0.1 M H_2SO_4 electrolyte at a potential scan rate of 50 mV s^{-1} to verify the long-range order of the electrode' s surface atoms.

Step b is cleaning the electrode in Ar (6N) purged UHP water thoroughly for the removal of sulphuric acid.

In step c, the electrode is immersed in 10 M NaOH. The application of a constant polarization potential from $E = 0.0$ V to a defined (85%) iR-compensated polarization potential limit E_p (in Fig. 11, $E_p = -1.0$ V), for a defined polarization time (in Fig. 11, t_p = 60.0 s).

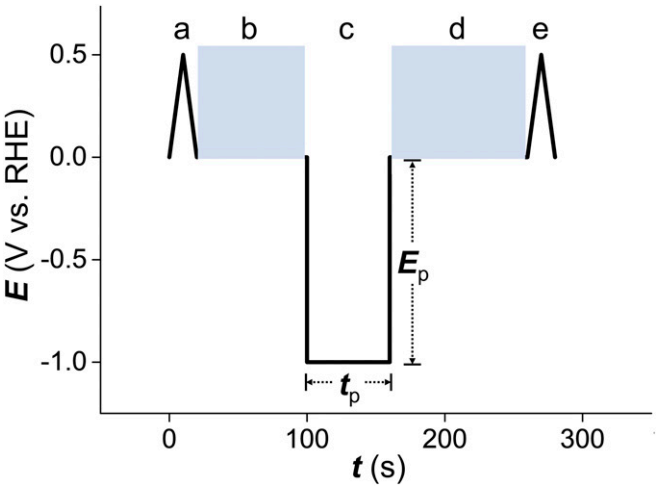

Fig. 11. The potential program employed in the cathodic corrosion studies and morphology examination. Step a is CV in hydrogen adsorption/desorption region in 0.1 M H_2SO_4 aqueous solution. Step b is cleaning the electrode in deoxygenated UHP water. Step c is cathodic corrosion in 10 M NaOH aqueous solution at a given potential E_p for a given time t_p. Step d is cleaning the electrode in deoxygenated UHP water. Step e is CV in hydrogen adsorption/desorption region in 0.1 M H_2SO_4 aqueous solution.

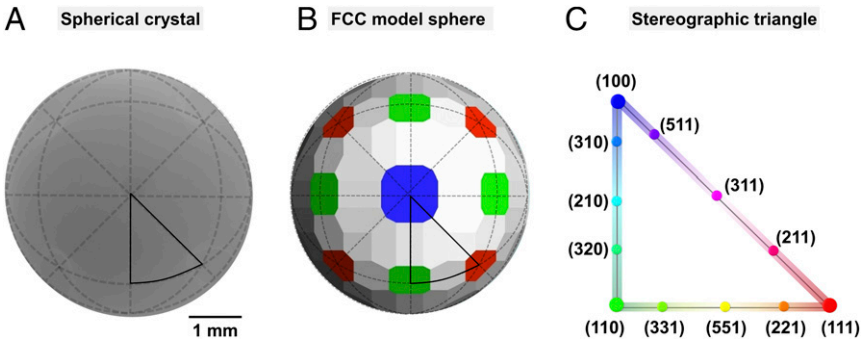

Fig. 12. The methodology of the Pt(spherical) electrode and surface facet identification. (*A*) An SEM image of an actual Pt(spherical) electrode. (*B*) An image of a simulated spherical Pt single crystal, with the low Miller index facets, depicted using different colors [i.e., (111) in red, (100) in blue, and (110) in green]. One stereographic triangle in these two images is marked using a black solid line. (*C*) Color-coded visualization of a stereographic triangle showing as filled, solid circles the location of 12 surface structures, which are the subject of our study.

Step d is cleaning the electrode in Ar (6N) purged UHP water thoroughly for the removal of sodium hydroxide.

Step e is acquisition of a CV profile in the 0.07 V $\leq E \leq$ 0.50 V range in a 0.1 M H_2SO_4 electrolyte at s = 50 mV s^{-1} to analyze surface structural changes in the monocrystalline Pt electrode brought about by the cathodic treatment.

Since the CV profile in H_2SO_4 in the 0.07 V $\leq E \leq$ 0.50 V range serves as an electrochemical fingerprint of the surface, a comparison of the CV profiles acquired before and after the cathodic treatment allows us to identify and quantify surface structural changes (25, 36, 37).

Microscopic Analysis of Cathodic Corrosion. Surface roughening of the monocrystalline Pt(*hkl*) electrodes brought about by the cathodic corrosion was analyzed using SEM (Apreo, Thermo Scientific) and AFM (JPK Nanowizard 4). The SEM is operated in a high-vacuum condition ($<1 \times 10^{-6}$ mbar), and the images are collected at a beam setting of 10 kV and 0.40 nA using an Everhart–Thornley detector. The AFM measurement is conducted in contact mode using a gold-coated tip (NANOSENSORS PPP-FMAuD; resonance frequency, 75 kHz; force constant, 2.8 N/m; tip radius of curvature < 50 nm) with a scan rate of 0.4 Hz.

After the corrosion experiment, the monocrystalline Pt electrode was carefully removed from the electrochemical cell and placed in a custom-made SEM/AFM sample holder. Then, the sample was rinsed under a stream of UHP water to remove acid from the electrode. Subsequently, the monocrystalline Pt(*hkl*) electrodes were dried in a high-purity Ar(g) stream and placed in the SEM/AFM chamber for analysis. When being transferred between the electrochemistry setup and the SEM instrument/AFM laboratory or when not being used, the sample was always stored using a custom-made vacuum container to minimize any exposure to the ambient environment.

To find the main surface facets in the Pt(spherical) electrode, we modeled a monocrystalline Pt sphere and compared it to an SEM image of Pt(spherical) electrode. Fig. 12*A* shows an SEM image of an actual monocrystalline Pt(spherical) electrode, and Fig. 12*B* presents an image of a simulated spherical Pt single crystal, with the low Miller index facets, depicted using different colors [i.e., (111) in red, (100) in blue, and (110) in green]. The modeled spherical single crystal is small (the number of atoms that can be modeled is limited); hence, not all facets are visible. In the actual and simulated images, stereographic triangles are superimposed using gray dashed lines. The SEM instrument was equipped with a three-axis goniometer and allowed us to orient the monocrystalline Pt(spherical) electrode and to acquire SEM images that were then superimposed on the simulated single crystal. Once superimposed with reasonable accuracy (±3°), we can identify the location of the main surface facets within the actual monocrystalline Pt(spherical) electrode. One stereographic triangle in the actual and simulated single crystals is marked with black solid lines; it contains all basal and stepped facets. Fig. 12*C* presents a color-coded visualization of this triangle and shows as solid circles the location of 12 surface structures, which are the subject of our study. As explained above, the low Miller index surfaces are marked by red, blue, and green filled circles at the vertices of the triangle; stepped surfaces are found along the lines. The stepped surfaces are color-coded as a combination of the colors used for the low Miller index surfaces (21).

Data Availability. Origin files and images have been deposited in Leiden Repository (https://openaccess.leidenuniv.nl/).

ACKNOWLEDGMENTS. This work received partial support from Hitachi High-Tech Corporation. Prof. Gregory Jerkiewicz (Queen's University, Canada) is acknowledged for knowledge transfer during the development of Pt spherical single crystal growth procedure.

1. F. Haber, Über Elektrolyse der Salzsäure nebst Mitteilungen über kathodische Formation von Blei. III. Mitteilung.*Z. Anorg. Chemie* **16**, 438–449 (1898).
2. A. I. Yanson *et al*., Cathodic corrosion: A quick, clean, and versatile method for the synthesis of metallic nanoparticles. *Angew. Chem. Int. Ed. Engl.* **50**, 6346–6350 (2011).
3. W. Huang, S. Chen, J. Zheng, Z. Li, Facile preparation of Pt hydrosols by dispersing bulk Pt with potential perturbations. *Electrochem. Commun.* **11**, 469–472 (2009).
4. P. Rodriguez, F. D. Tichelaar, M. T. M. Koper, A. I. Yanson, Cathodic corrosion as a facile and effective method to prepare clean metal alloy nanoparticles. *J. Am. Chem. Soc.* **133**, 17626–17629 (2011).
5. J. Fichtner *et al*., Top-down synthesis of nanostructured platinum-lanthanide alloy oxygen reduction reaction catalysts: Pt $_x$Pr/C as an example. *ACS Appl. Mater. Interfaces* **11**, 5129–5135 (2019).
6. M. L. Kromer *et al*., High-throughput preparation of metal oxide nanocrystals by cathodic corrosion and their use as active photocatalysts. *Langmuir* **33**, 13295–13302 (2017).
7. A. I. Yanson, P. V. Antonov, Y. I. Yanson, M. T. M. Koper, Controlling the size of platinum nanoparticles prepared by cathodic corrosion. *Electrochim. Acta* **110**, 796–800 (2013).
8. Y.-G. Kim, J. H. Baricuatro, A. Javier, J. M. Gregoire, M. P. Soriaga, The evolution of the polycrystalline copper surface, first to Cu, (111) and then to Cu(100), at a fixed CO 2 RR potential: A study by operando EC-STM. *Langmuir* **30**, 15053–15056 (2014).
9. B. Vanrenterghem *et al*., Cutting the Gordian Knot of electrodeposition via controlled cathodic corrosion enabling the production of supported metal nanoparticles below 5 nm. *Appl. Catal. B* **226**, 396–402 (2018).
10. T. J. P. Hersbach, V. A. Mints, F. Calle-Vallejo, A. I. Yanson, M. T. M. Koper, Anisotropic etching of rhodium and gold as the onset of nanoparticle formation by cathodic corrosion. *Faraday Discuss.* **193**, 207–222 (2016).
11. T. J. P. Hersbach, A. I. Yanson, M. T. M. Koper, Anisotropic etching of platinum electrodes at the onset of cathodic corrosion. *Nat. Commun.* **7**, 12653 (2016).
12. J. Feng *et al*., Cathodic corrosion of a bulk wire to nonaggregated functional nanocrystals and nanoalloys. *ACS Appl. Mater. Interfaces* **10**, 9532–9540 (2018).
13. T. J. P. Hersbach, R. Kortlever, M. Lehtimäki, P. Krtil, M. T. M. Koper, Local structure and composition of PtRh nanoparticles produced through cathodic corrosion. *Phys. Chem. Chem. Phys.* **19**, 10301–10308 (2017).
14. T. J. P. Hersbach *et al*., Alkali metal cation effects in structuring Pt, Rh, and Au surfaces through cathodic corrosion. *ACS Appl. Mater. Interfaces* **10**, 39363–39379 (2018).
15. A. I. Yanson, P. V. Antonov, P. Rodriguez, M. T. M. Koper, Influence of the electrolyte concentration on the size and shape of platinum nanoparticles synthesized by cathodic corrosion. *Electrochim. Acta* **112**, 913–918 (2013).
16. Y. I. Yanson, A. I. Yanson, Cathodic corrosion. I. Mechanism of corrosion via formation of metal anions in aqueous medium. *Low Temp. Phys.* **39**, 304–311 (2013).
17. A. I. Yanson, Y. I. Yanson, Cathodic corrosion. II. Properties of nanoparticles synthesized by cathodic corrosion. *Low Temp. Phys.* **39**, 312–317 (2013).
18. M. Elwenspoek, H. V. Jansen, *Silicon Micromachining* (Cambridge University Press, ed. 1, 2004).
19. R. C. Salvarezza, A. J. Arvia, "A modern approach to surface roughness applied to electrochemical systems" in *Modern Aspects of Electrochemistry*, B. E. Conway, J. O. Bockris, R. E. White, Eds. (Springer, Boston, MA, ed. 28, 1996), pp. 289–373.

20. N. Furuya, M. Shibata, Structural changes at various Pt single crystal surfaces with potential cycles in acidic and alkaline solutions. *J. Electroanal. Chem. (Lausanne)* **467**, 85–91 (1999).
21. N. Arulmozhi, D. Esau, R. P. Lamsal, D. Beauchemin, G. Jerkiewicz, Structural transformation of monocrystalline platinum electrodes upon electro-oxidation and electro-dissolution. *ACS Catal.* **8**, 6426–6439 (2018).
22. M. Ruge *et al*., Electrochemical oxidation of smooth and nanoscale rough Pt(111): An in situ surface X-ray scattering study. *J. Electrochem. Soc.* **164**, H608–H614 (2017).
23. J. H. Baricuatro, Y.-G. Kim, C. L. Korzeniewski, M. P. Soriaga, Seriatim ECSTM-ECPMIRS of the adsorption of carbon monoxide on Cu(100) in alkaline solution at CO2-reduction potentials. *Electrochem. Commun.* **91**, 1–4 (2018).
24. V. Climent, J. Feliu, Single crystal electrochemistry as an in situ analytical characterization tool. *Annu. Rev. Anal. Chem. (Palo Alto Calif.)* **13**, 201–222 (2020).
25. J. Solla-Gullón, P. Rodríguez, E. Herrero, A. Aldaz, J. M. Feliu, Surface characterization of platinum electrodes. *Phys. Chem. Chem. Phys.* **10**, 1359–1373 (2008).
26. G. A. Attard, A. Brew, Cyclic voltammetry and oxygen reduction activity of the Pt {110}-(1×1) surface. *J. Electroanal. Chem. (Lausanne)* **747**, 123–129 (2015).
27. J. I. Goldstein *et al*., *"High resolution imaging" in Scanning Electron Microscopy and X-Ray Microanalysis*, J. I. Goldstein, Ed. *et al.* (Springer, New York, ed. 4, 2018), pp. 147–164.
28. P. Meakin, *Fractals, Scaling and Growth Far from Equilibrium* (Cambridge University Press, 1998).
29. Z. Zhang, M. G. Lagally, Atomistic processes in the early stages of thin-film growth. *Science* **276**, 377–383 (1997).
30. D. Geng *et al*., Fractal etching of graphene. *J. Am. Chem. Soc.* **135**, 6431–6434 (2013).
31. M. H. Richter, M. Lublow, K. M. Papadantonakis, N. S. Lewis, H.-J. Lewerenz, Genesis and propagation of fractal structures during photoelectrochemical etching of n-silicon. *ACS Appl. Mater. Interfaces* **12**, 17018–17028 (2020).
32. N. Arulmozhi, D. Esau, J. van Drunen, G. Jerkiewicz, Design and development of instrumentations for the preparation of platinum single crystals for electrochemistry and electrocatalysis research part 3: Final treatment, electrochemical measurements, and recommended laboratory practices. *Electrocatalysis* **9**, 113–123 (2018).
33. S. Cherevko, A. R. Zeradjanin, G. P. Keeley, K. J. Mayrhofer, A comparative study on gold and platinum dissolution in acidic and alkaline media. *J. Electrochem. Soc.* **161**, H822–H830 (2014).
34. N. Arulmozhi, G. Jerkiewicz, Design and development of instrumentations for the preparation of platinum single crystals for electrochemistry and electrocatalysis research, Part 1: Semi-automated crystal growth. *Electrocatalysis* **7**, 507–518 (2016).
35. N. Arulmozhi, G. Jerkiewicz, Design and development of instrumentations for the preparation of platinum single crystals for electrochemistry and electrocatalysis research, Part 2: Orientation, cutting, and annealing. *Electrocatalysis* **8**, 399–413 (2017).
36. N. Furuya, S. Koide, Hydrogen adsorption on platinum single-crystal surfaces. *Surf. Sci.* **220**, 18–28 (1989).
37. F. Sugimura, M. Nakamura, N. Hoshi, The oxygen reduction reaction on kinked stepped surfaces of Pt. *Electrocatalysis* **8**, 46–50 (2017).